References

[1]Hixon, R., "On Increasing the Accuracy of MacCormack Schemes for Aeroacoustic Applications," AIAA Paper 97-1586, 1997.

[2]Lele, S. K., "Compact Finite Difference Schemes with Spectral Like Resolution," *Journal of Computational Physics*, Vol. 103, 1992, pp. 16–42.

[3]Tam, C. K. W., and Webb, J. C., "Dispersion Relation Preserving Schemes for Computational Acoustics," *Journal of Computational Physics*, Vol. 107, No. 2, 1993, pp. 262–281.

[4]Gottlieb, D., and Turkel, E., "Dissipative Two-Four Method for Time Dependent Problems," *Mathematics of Computations*, Vol. 30, No. 136, 1976, pp. 703–723.

[5]Thompson, K. W., "Time-Dependent Boundary Conditions for Hyperbolic Systems," *Journal of Computational Physics*, Vol. 68, No. 1, 1987, pp. 1–24.

[6]Bayliss, A., and Turkel, E., "Far Field Boundary Conditions for Compressible Flows," *Journal of Computational Physics*, Vol. 48, Nov. 1982, pp. 182–199.

[7]Streett, C. L., and Macaraeg, M. G., "Spectral Multi-Domain for Large Scale Fluid Dynamics Simulations," *International Journal for Applied Numerical Mathematics*, Vol. 6, 1989, pp. 123–139.

[8]Hu, F. Q., "On Absorbing Boundary Conditions for Linearized Euler Equations by a Perfectly Matching Layer," Inst. for Computer Applications in Science and Engineering, ICASE Rept. 95-70, Hampton, VA, 1995.

[9]Mankbadi, R. R., Hayder, M. E., and Povinelli, L. A., "Structure of Supersonic Jet Flow and Its Radiated Sound," *AIAA Journal*, Vol. 32, No. 5, 1994, pp. 897–906.

[10]Owis, F., and Balakumar, P., "Evaluation of Boundary Conditions and Numerical Schemes for Jet Noise Computations," AIAA Paper 2000-0920, Jan. 2000.

P. J. Morris
Associate Editor

Compressible Dynamic Stall Control Using Dynamic Shape Adaptation

M. S. Chandrasekhara*
Naval Postgraduate School, Monterey, California 93943
and
M. C. Wilder† and L. W. Carr‡
NASA Ames Research Center, Moffett Field, California 94035

Nomenclature

C_p	=	pressure coefficient
$C_{p_{\min}}$	=	peak suction pressure coefficient
c	=	airfoil chord
f	=	frequency of oscillation, Hz
k	=	reduced frequency, $\pi f c/U_\infty$
M	=	freestream Mach number
p	=	static pressure
s, n	=	coordinates along and normal to airfoil surface
x, y	=	chordwise and vertical distance
α	=	angle of attack
α_0	=	mean angle of attack
Ω	=	spanwise component of vorticity

I. Introduction

IT was shown in earlier work[1] on unsteady separation control that changing the leading edge curvature of an NACA 0012 airfoil was effective in producing significant stall delay (about 5 deg at $M = 0.3$) through decreasing leading-edge flow acceleration. The extreme sensitivity of the airfoil peak suction pressure to the flow acceleration around the airfoil leading edge resulted in reduced peak suction levels when the nose radius was increased. Rounding the leading edge also distributed the low-pressure region over a wider extent on the airfoil upper surface, reducing the leading-edge adverse pressure gradient, thus making it possible for the airfoil to reach higher angles of attack before stalling, in both steady and unsteady flows. As a result, satisfactory airfoil performance ensued over a larger operating envelope. In Ref. 1, certain intermediate shapes are identified that were dynamic stall vortex free. The redistribution of the vorticity flux arising from tailoring the nose radius can eliminate the dynamic stall vortex completely and vastly improve a pitching airfoil force and moment loops. Thus, such a flow control method is very valuable for compressible dynamic stall control, which is always a leading-edge type of stall, dominated by a strong clockwise vortex convecting over the airfoil.

Although in Ref. 1 control of compressible dynamic stall using fixed, round nosed airfoils was demonstrated, rotor applications require dynamic airfoil shape adaptation because of the large differences in flow speeds on the advancing and retreating sides. Furthermore, the U.S. Army has stipulated that the next generation of helicopters be significantly more capable in terms of load capacity and maneuverability. This requires removing the constraints imposed by the onset of dynamic stall to enlarge the flight envelope. One way a given rotor blade can deliver improved performance is if the potential flowfield over it is suitably altered, so that it can respond to the rapidly changing flow conditions as it flies through a cycle. It is proposed here to use dynamic shape adaptation as a means to achieve this and to avoid compressible dynamic stall on its retreating side. Proper blade adaptation requires determining the shapes that the airfoil can take without stalling during such a maneuver. These shapes depend on the conditions encountered by the rotor blade. To satisfactorily employ this technique, the fluid mechanics of the flow over airfoils of different shapes need to be understood, and have been discussed in Ref. 1.

The present experiments were focused on controlling the flow over a sinusoidally oscillating airfoil by determining the dynamic shape variations that produced the right nose curvature at each instantaneous flow condition, thus producing the most attached flow over the range of angles of attack of interest. A sharp-to-round shape change profile was chosen, while always maintaining the airfoil shapes within the range of a previously determined attached flow envelope,[1] to achieve the desired flow control effect.

II. Description of the Experiment

Practical implementation of real-time adaptation of an oscillating airfoil requires overcoming the demanding challenges of design and fabrication. A NACA 0012 derivative airfoil, known as the dynamically deforming leading edge (DDLE) airfoil, with 15.24-cm chord was specially developed for the present purpose. Its leading 20% is cast from a carbon–fiber composite; the rest is machined from solid metal. The composite fiber is about 50 μm thick at the leading edge and is attached with a tang to a mandrel, shaped to the NACA 0012 profile, housed inside the airfoil. The mandrel, driven by brushless servomotors, translates in the chordwise direction by less than 2 mm to produce up to 320% continuous change in the airfoil leading-edge radius. For convenience, the various shapes used are denoted by integers, with 75-μm mandrel displacement for each shape number change. Shape 0 corresponds to the NACA 0012 profile. More details about the DDLE airfoil design may be found in Ref. 2.

A typical deformation schedule consists of rounding the nose by retracting the leading edge, holding the final shape for a dwell period, and extending the leading edge back to the original shape. As stated earlier, prior studies[1] identified dynamic stall vortex-free geometries, based on which oscillating airfoil shape-change schedules that offered the most potential for success were determined. Two shape-change schedules, one fast and the other slow, along with the corresponding angle-of-attack variations, shown in Fig. 1, were used in this study (for details, see Ref. 3). The oscillations in

Received 14 July 1999; revision received 26 February 2001; accepted for publication 18 June 2001.

*Research Professor and Associate Director, Navy–NASA Joint Institute of Aeronautics, Department of Aeronautics and Astronautics; mailing address: NASA Ames Research Center, M.S. 260-1, Moffett Field, CA 94035-1000. Associate Fellow AIAA.

†Research Scientist, Reactive Flow Environments Branch. Member AIAA.

‡Emeritus Scientist, Aeroflightdynamics Directorate, U.S. Army Aviation and Missile Command and Experimental Physics Branch. Senior Member AIAA.

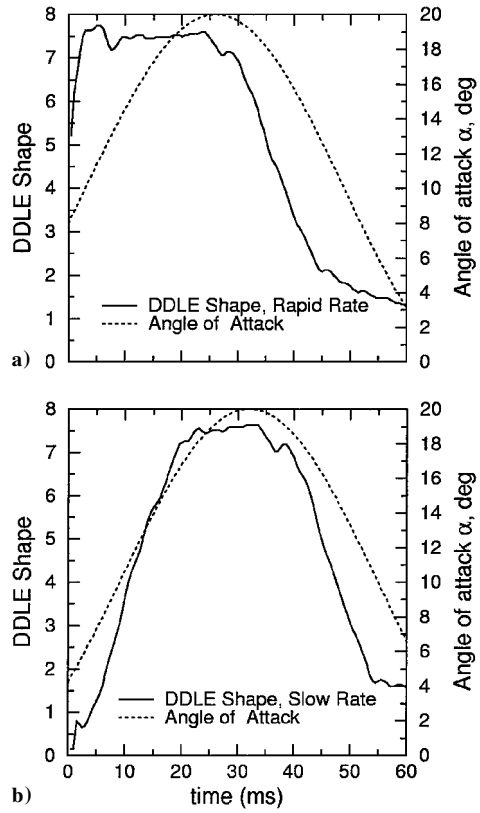

Fig. 1 DDLE shape and angle-of-attack history; $M = 0.3$ and $k = 0.05$: a) rapid adaptation and b) slow adaptation.

the output response of the feedback system were minimized during the system tuning process for each condition to maintain the DDLE airfoil shape to within a half-integer of the final round shape during deformation.

Point diffraction interferometry (PDI) was used to record flow images at specific angles of attack as the DDLE airfoil was dynamically deformed while oscillating as $\alpha = 10 + 10 \sin \omega t$ deg, at $M = 0.3$ and $k = 0.05$. The instantaneous DDLE position (shape) encoder values were recorded for each image using custom phase-locking circuitry to include the effect of the two independent timescales (the airfoil reduced frequency and the dynamic shape-change rate) present in this flow.[3] The PDI images were initially evaluated qualitatively. Quantitative analysis was conducted using in-house developed software under isentropic flow assumptions to obtain the pressures where applicable.

The estimated uncertainties in the data are as follows: Mach number, ±0.005; angle of attack, 0.05 deg; reduced frequency, 0.005; airfoil shape, 0.05; airfoil displacement, 4 μm; C_p, ±0.1; $C_{p_{\min}}$, −0.5; $dC_p/d(x/c)$, ±25; and change in α during DDLE movement, ±0.25 deg.

III. Results and Discussion

A. Qualitative Description of the Flow

Figure 2 presents 12 interferograms recorded at different angles of attack for the shape adapting while pitching (SAP) airfoil at $M = 0.3$ and $k = 0.05$ for the fast schedule used. It is clear from the fringe pattern in Fig. 2a that the flow is fully attached at $\alpha = 12.03$ deg, for shape 2. Attached flow is also seen in Figs. 2b and 2c for $\alpha = 14$ and 15 deg, respectively, for shape −7.5, although some disturbance is noticeable in Fig. 2c near $x/c \approx 0.1$. Results presented in Ref. 1 show that the flow over the fixed, shape 8.5, airfoil generally behaves similarly to that seen in Fig. 2 with slight differences in the angle of attack of the events. Note that on a NACA 0012 airfoil, dynamic stall onset occurs at $\alpha = 14$ deg at $M = 0.3$. In contrast, on the SAP airfoil, the flow appears fully attached even at $\alpha = 16$ deg (Fig. 2d), highlighting one benefit of dynamic shape adaptation. Traces of trailing-edge separation are present in Fig. 2e for $\alpha = 17$ deg over the shape 7 airfoil, which become more pronounced for $\alpha = 18$ deg (Fig. 2f) and for $\alpha = 19$ deg (Fig. 2g). A look at the leading-edge image reveals the presence of a large number of fringes in the flow, indicating the continued development of strong leading-edge suction, even when trailing-edge separation has progressed up to $x/c \approx 0.1$ on the upper surface. At $\alpha = 20$ deg (Fig. 2h), the maximum number of fringes has decreased, and hence, the peak suction pressure has dropped from that observed in Fig. 2g, but the leading-edge flow remains attached. During the downstroke, the flow at $\alpha = 19$ deg (Fig. 2i) and $\alpha = 18$ deg (Fig. 2j) appears similar to that seen on the upstroke at these angles, the only difference being that the maximum number of leading-edge fringes is smaller on the downstroke. As the return to the original airfoil shape begins, light dynamic stall is induced at $\alpha = 16$ deg, (Fig. 2k) in much the same way as was seen for the fixed shape 8.5 airfoil.[1] This is because the flow has to adjust to the more favorable conditions, in particular to the lower levels of vorticity flux associated with these lower angles of attack, to prevent buildup of vorticity. Most interesting, fully reattached flow develops at the high angle of attack of 15 deg on the downstroke for the shape 5 airfoil, and the suction peak becomes well established again. In contrast, at this angle of attack, light dynamic stall was present in the flow over

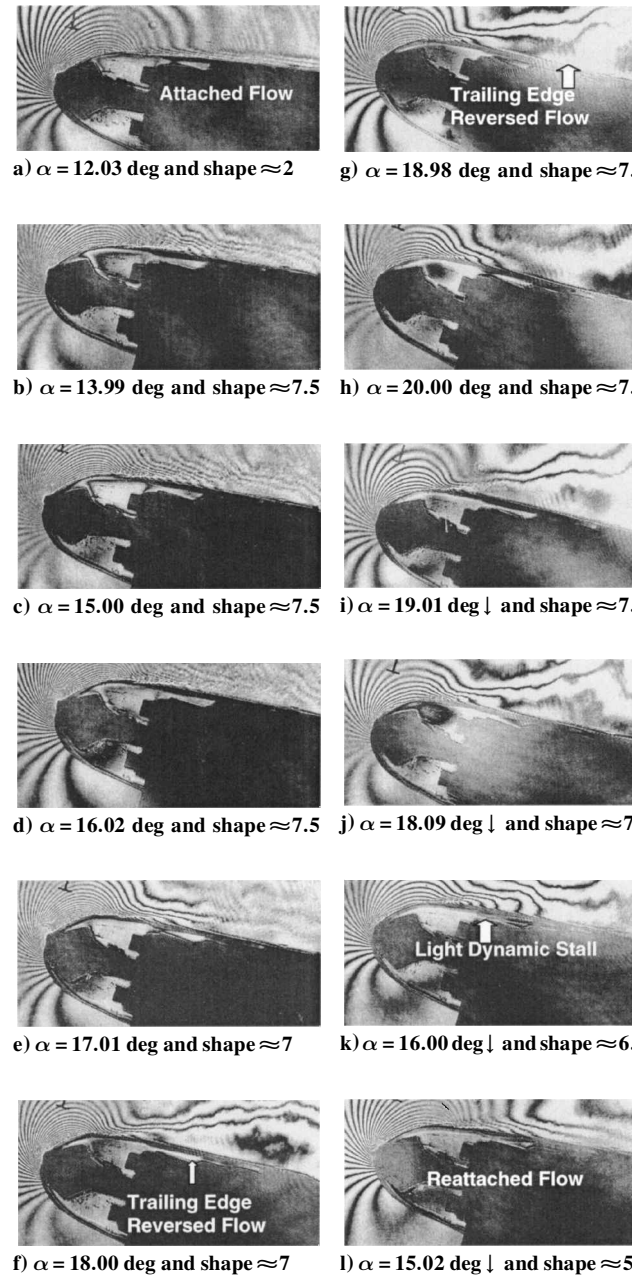

a) $\alpha = 12.03$ deg and shape ≈2
g) $\alpha = 18.98$ deg and shape ≈7.5
b) $\alpha = 13.99$ deg and shape ≈7.5
h) $\alpha = 20.00$ deg and shape ≈7.5
c) $\alpha = 15.00$ deg and shape ≈7.5
i) $\alpha = 19.01$ deg ↓ and shape ≈7.5
d) $\alpha = 16.02$ deg and shape ≈7.5
j) $\alpha = 18.09$ deg ↓ and shape ≈7
e) $\alpha = 17.01$ deg and shape ≈7
k) $\alpha = 16.00$ deg ↓ and shape ≈6.5
f) $\alpha = 18.00$ deg and shape ≈7
l) $\alpha = 15.02$ deg ↓ and shape ≈5

Fig. 2 PDI images of flow over the SAP airfoil; $M = 0.3$, $k = 0.05$, and rapid adaptation.

the fixed shape 8.5 airfoil as reported in Ref. 1, leading to the conclusion that the SAP airfoil is better than a fixed shape 8.5 airfoil. Figure 2 also shows that it is possible to manipulate the flowfield to keep the leading-edge flow attached throughout the oscillation cycle. Similar results were also obtained for the slow schedule.

The major difference between the NACA 0012 airfoil and the dynamically adapted airfoil flowfields is the absence of the dynamic stall vortex for the latter case. Thus, it is clear that the vorticity fields in the two cases are also different. The absence of the dynamic stall vortex leads to the deduction that the pitching moment variations over the SAP airfoil will be much milder, and the range of angles of attack over which the flow remains attached will also be considerably larger when compared to the NACA 0012 airfoil. Dynamic shape adaptation has successfully altered the flow vorticity field, leading to changes in the airfoil stall behavior from leading-edge type to the trailing-edge type. If the timescale of airfoil oscillation and airfoil adaptation can be carefully matched to diffuse the excess vorticity on the downstroke, then it may even be possible to avoid the light dynamic stall condition encountered normally. This requires returning to the original shape very slowly. However, because the airfoil oscillation frequency is derived from a rotor flow condition, the airfoil adaptation rates are bounded. Hence, attempts to eliminate the light dynamic stall state may be impractical in real use.

B. Peak Suction Development

In Fig. 3, the development of the airfoil peak suction pressure coefficient $C_{p_{\min}}$ is compared for the NACA 0012, fixed shape 8.5, and the SAP airfoil geometries at the two deformation rates used. Within experimental uncertainty, the peak suction values for the two deformation rates show nearly the same variation, even though the shape adaptation was initiated at different angles of attack. The NACA 0012 airfoil generates the highest value of $C_{p_{\min}}$ (≈ -7.5), which indicates that the flow has become locally supersonic ($C_{p_{\text{crit}}} \approx -7.0$ at $M = 0.3$); however, no shocks are seen. In both the fixed-shape case and the SAP case, $C_{p_{\min}}$ just reaches the critical value with the fixed shape 8.5 airfoil showing a slightly more gradual fall of peak suction pressure. On the upstroke, the values for the SAP airfoil are slightly higher, suggesting that the suction lift over it tends to be marginally higher. Of greater interest is the 30% smaller size of the peak suction pressure loop for both the SAP cases. This difference between the fixed shape 8.5 and SAP airfoil cases in both the upstroke and downstroke peak suction pressures is due to the different extents of trailing-edge separation present over the airfoils because there was no dynamic stall vortex in both flows. Because the flow reattaches at $\alpha = 15$ deg for the SAP cases, as opposed to at $\alpha \approx 12$ deg for the fixed shape 8.5 case, its loop is smaller. In contrast, for the NACA 0012 airfoil, the shedding of the large dynamic stall vortex causes the flow to separate completely. Complete reattachment does not occur until $\alpha \approx 8$ deg on the downstroke.[4] The large $\Delta\alpha$ between separation and reattachment results in a very large hysteresis loop in the moment coefficient as well. If shape adaptation were ideal and complete, a difference in the $C_{p_{\min}}$ development between the upstroke and downstroke would not be present because the flow vorticity would be diffused through the boundary layer at a rate consistent with its production throughout the oscillation cycle. This should indeed be the goal of shape adaptation. In reality, one can only expect to minimize the hysteresis loop so that the airfoil can deliver a performance that is free from large-scale separation effects. The results presented here confirm that satisfactory shape adaptation was achieved for this experimental condition of $M = 0.3$ and $k = 0.05$.

Note that the shape adaptation for the slow case was initiated at $\alpha \approx 3.8$ deg and for the rapid case at $\alpha \approx 8$ deg, these angles being determined from the attached flow envelope developed in earlier studies. The primary factor that controls the shape-change schedule is the attached flow envelope for each Mach number. The requirement to satisfy, for potential success, is that any instantaneous shape reached should be within this envelope for the flow at any angle to remain attached. The delay in pressure field development produced due the lag effects of unsteady flow provides some latitude in this regard.

It was also observed in these studies that initiating the deformation at inappropriate angles of attack induced premature dynamic stall. Thus, it is very important to determine the attached flow envelope in steady flow first, before proceeding with dynamic stall flow control. More details on this can be found in Ref. 3.

C. Vorticity Flux Distributions

The vorticity fluxes calculated from the PDI derived pressure distributions[1] for the fixed shape 8.5 and the SAP airfoils are compared in Fig. 4. The large changes in the potential flow due to large real-time geometry modifications translate to a large effect on the pressure distribution, which should be seen in the vorticity flux also. At $\alpha = 15$ deg, the vorticity flux over the rapidly adapted SAP airfoil is generally lower than that over the fixed shape 8.5 airfoil. The location of the peak vorticity flux value over the SAP airfoil moves toward the trailing edge at $x/c \approx 0.08$ (Fig. 4a). No comparisons can be made with the distributions for the NACA 0012 airfoil because dynamic stall occurs at $\alpha = 14$ deg, and the flow separates completely by $\alpha = 16$ deg. However, in Ref. 1 it was shown that the vorticity flux distributions over the fixed shape 8.5 airfoil were significantly superior to that over the NACA 0012 airfoil at the lower angles of attack because of its lower maximum value and downstream location of the peaks.

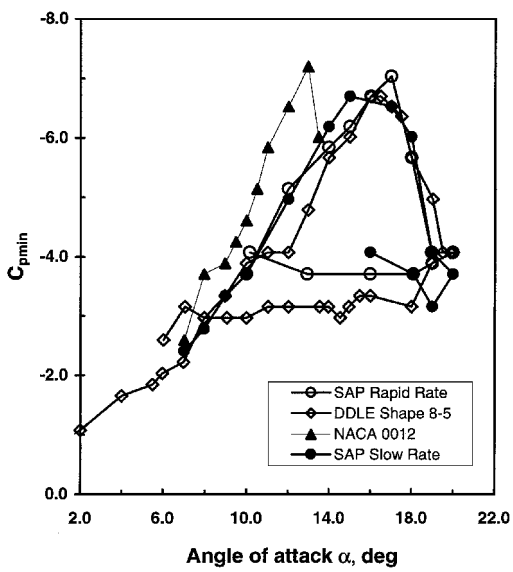

Fig. 3 Comparison of peak suction development over the SAP, shape 8.5 and NACA 0012 airfoils; $M = 0.3$ and $k = 0.05$.

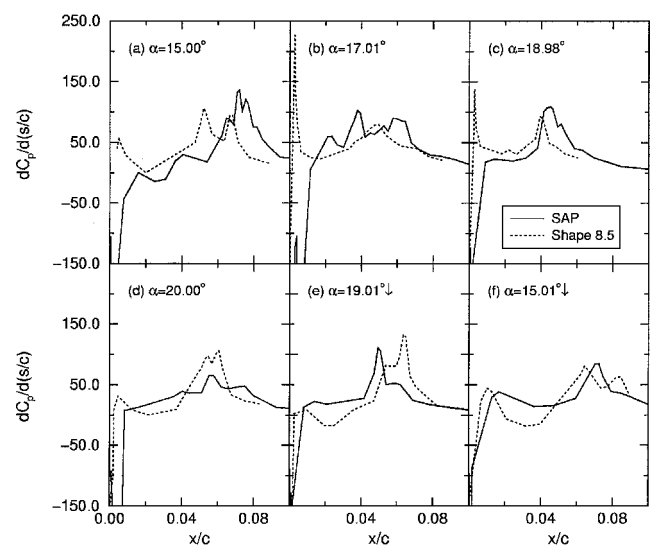

Fig. 4 Vorticity flux development over the shape 8.5 and SAP airfoils; $M = 0.3$ and $k = 0.05$.

Figure 4 establishes that the SAP airfoil flow is generally better than that of the fixed shape 8.5 airfoil on the upstroke. The peak vorticity flux for the SAP airfoil moves slightly upstream with increasing angle of attack (from $x/c = 0.08$ to 0.05; Figs. 4b–4d), but it is lower than that for the shape 8.5 airfoil. The large peak of 225 seen for the fixed shape 8.5 airfoil close to the leading edge in Fig. 4b is not observed for the SAP airfoil, even though its instantaneous shape of 7.5 attained dynamically is very close to the fixed shape 8.5. This can be attributed to the extreme sensitivity of the flow to the dynamic change of leading-edge curvature. At $\alpha = 20$ deg (Fig. 4d), the peak vorticity in the SAP airfoil flow drops to about 50% of that seen in the fixed shape 8.5 airfoil flow, occurring at $x/c = 0.05$. In this, the peak vorticity occurs away from the leading edge and is significantly lower, when compared to the NACA 0012 airfoil before onset of dynamic stall. This explains why no dynamic stall vortex was observed in the deforming airfoil flow. On the downstroke at $\alpha = 19$ deg (Fig. 4e), the SAP airfoil flow vorticity level is somewhat higher and leads the fixed shape 8.5 airfoil, a trend that can be traced to the peak suction pressure being higher during the downstroke for the SAP airfoil. In Fig. 4f, the values for the fixed shape 8.5 airfoil are compared at $\alpha = 15.5$ deg with the SAP airfoil at $\alpha = 15$ deg. The higher vorticity flux levels suggest that a somewhat improved lift performance can be expected from the SAP airfoil due to the increased circulation due to this vorticity.

IV. Conclusions

1) Compressible dynamic stall has been successfully controlled using dynamic shape adaptation. This required a very small (0.6-mm) change in the chord length of a dynamically adaptive airfoil that produced a nearly 150% change in the leading-edge radius of curvature.

2) The flow was found to be dynamic stall vortex free for $M = 0.3$, $k = 0.05$, and $\alpha = 10 + 10 \sin \omega t$ deg. The favorable effects of dynamic shape adaptation realized through changes in the instantaneous potential flow resulted in broader pressure distributions with lower peak suction values and led to a redistribution of the unsteady flow vorticity. The vorticity levels decreased to values where the dynamic stall vortex did not form.

3) The peak suction variation loop over the oscillation cycle was found to be the smallest for the adapting airfoil.

4) The deformation rate, the initiation angle of attack, and the amount of nose curvature change affect the success of the approach significantly. The most benefit is produced while remaining within the attached flow envelope for a given Mach number during dynamic shape adaptation.

Acknowledgments

This work was supported by a Research Grant (MIPR8BNP-SARO07) from the U.S. Army Research Office and was monitored by T. L. Doligalski. The support of S. S. Davis, Fluid Mechanics Laboratory of NASA Ames Research Center, the assistance of R. A. Miller in model installation, and the control system design effort of D. D. Squires and M. Khov, Sverdrup Technology, Inc., are gratefully acknowledged.

References

[1]Chandrasekhara, M. S., Wilder, M. C., and Carr, L. W., "Unsteady Stall Control Using Dynamically Deforming Airfoils," *AIAA Journal*, Vol. 36, No. 3, 1998, pp. 1792–1800.

[2]Chandrasekhara, M. S., Carr, L. W., Wilder, M. C., Sticht, C. D., and Paulson, G. N., "Design and Development of a Dynamically Deforming Leading Edge Airfoil for Unsteady Flow Control," *ICIASF'97 RECORD*, IEEE Publication 97CH36121, Inst. of Electrical and Electronics Engineers, Piscataway, NJ, 1997, pp. 132–140.

[3]Chandrasekhara, M. S., Carr, L. W., and Wilder, M. C., "Compressible Dynamic Stall Control Using a Shape Adaptive Airfoil," AIAA Paper 99-0650, Jan. 1999.

[4]Ahmed, S., and Chandrasekhara, M. S., "Reattachment Studies of an Oscillating Airfoil Dynamic Stall Flowfield," *AIAA Journal*, Vol. 32, No. 5, 1994, pp. 1006–1012.

A. Plotkin
Associate Editor

Flexibility Equations for Active Rack Isolation System Umbilicals with Planar End Loading

R. David Hampton*
U.S. Military Academy, West Point, New York 10996
Naveed Quraishi†
NASA Johnson Space Center, Houston, Texas 77058
and
Jason K. Rupert‡
Dynetics, Inc., Huntsville, Alabama 35806

Introduction

THE Active Rack Isolation System (ARIS) serves as the central component of an integrated, station-wide strategy to isolate microgravity space-science experiments on the International Space Station (ISS). ARIS uses 8 electromechanical actuators to isolate an International Standard Payload Rack (ISPR) from disturbances due to the motion of the ISS; 11 ARIS racks are being developed for the ISS. Disturbances to microgravity experiments on ARIS-isolated racks are transmitted primarily via the (nominally 13) ARIS umbilicals, which provide power, data, vacuum, cooling, and other miscellaneous services to the experiments. The two power umbilicals and, to a lesser extent, the vacuum umbilical, serve as the primary transmission path for acceleration disturbances. Experimental tests conducted by the ARIS team[1] (December 1998) indicate that looped power umbilicals resonate at about 10 Hz; unlooped power umbilicals resonate at about 4 Hz. In either case, the ARIS controller's limited bandwidth (about 2 Hz) admits only limited active isolation at these frequencies. Reduction in the umbilical resonant frequencies could help to address this problem.

Analytical studies of the nonlinear bending and deflection of a flexible, linearly elastic, fixed-end, cantilever beam (originally horizontal) have been conducted for a variety of loading conditions, including concentrated terminal transverse (vertical) loading[2–6]; uniformly distributed vertical loading[2,7–9]; uniformly distributed normal loading[10]; concentrated terminal inclined loading[11,12]; multiple concentrated vertical loads[13]; concentrated terminal vertical and moment loading[13]; and heavy, rigid, end-attachment loading.[14] Reference 15 provided a set of nonlinear equations for the case of a weightless flexible beam, with arbitrary, discrete, in-plane loads and boundary conditions. Typical exact solutions of beam deflections involve complete and incomplete elliptic integrals (for example, Refs. 2, 4–6, 13, and 14). For literature reviews, see Refs. 16–18.

In the special case of general terminal in-plane loading, that is, including both inclined-force and moment loads, in-plane flexibility (or stiffness) equations would be of particular interest toward umbilical design for microgravity-isolation purposes. The equations could be used to help optimize umbilical flexibilities and resonant frequencies for microgravity applications.

This Note develops equations for the in-plane deflections and flexibilities of an idealized umbilical (thin, flexible, prismatic, linearly elastic, fixed-end, cantilevered, with equal tensile and compressive moduli of elasticity) under terminal in-plane loading (inclined-force and moment). The effect of gravity can be neglected due to the on-orbit application. (Note that the deflection analysis is a special case of the treatment presented in Ref. 15.) The deflection and flexibility

Received 18 September 2000; revision received 18 June 2001; accepted for publication 20 June 2001.

*Associate Professor, Department of Civil and Mechanical Engineering. Member AIAA.

†Program Manager for the Active Rack Isolation System International Space Station Characterization Experiment, Payloads Office. Member AIAA.

‡Engineer, Missile Systems Department, Simulation and Analysis Section. Member AIAA.